Affordable omnidirectional subsurface extended image volumes

Tristan van Leeuwen[1], Rajiv Kumar[2] and Felix J. Herrmann[2]

[1] *Mathematical Institute, Utrecht University, The Netherlands,*

[2] *Dept. of Earth Ocean and Atmospheric Sciences, University of British Columbia, Vancouver, BC, Canada*

Email : T.vanLeeuwen@uu.nl, rkumar@eos.ubc.ca, fherrmann@eos.ubc.ca

(May 6, 2015)

Running head: **Efficient extended imaging**

ABSTRACT

Image gathers as a function of subsurface offset are an important tool for the inference of rock properties and velocity analysis in areas of complex geology. Traditionally, these gathers are thought of as multidimensional correlations of the source and receiver wavefields. The bottleneck in computing these gathers lies in the fact that one needs to store, compute, and correlate these wavefields in order to obtain the desired image gathers. Therefore, the image gathers are typically only computed for a limited number of subsurface points and for a limited range of subsurface offsets. In this paper, we offer a new perspective on such gathers by organizing the extended image, as a function of all subsurface offsets and all subsurface points, into a matrix whose $(i,j)^{\text{th}}$ entry captures the interaction between gridpoints i and j. Of course, it is infeasible to form and store this matrix explicitly. Instead, we propose an efficient algorithm to glean information from the image volume via matrix-

vector products, which can be computed efficiently. The probing techniques have two main advantages; *i)* by using all subsurface offsets, we can handle complex geological structures with steep dips, *ii)* we can probe the whole model simultaneously and do not have to pick points at which to compute the image gathers. We illustrate these advantages using two important applications of image gathers: amplitude-versus-angle reflectivity analysis and migration velocity analysis.

INTRODUCTION

Seismic reflection data are a rich source of information about the subsurface and by studying both dynamic and kinematic properties of the data we can infer both large-scale velocity variations as well as local rock properties. While the seismic data volume – as function of time, source and receiver positions – contains all necessary information, it is often more convenient to map all the relevant events to their respective positions in the subsurface. This leads to the definition of an *image volume* or *extended image* – as a function of depth, lateral position and some redundant spatial coordinate(s) – that has the same (or higher) dimensionality as the data volume. This mapping can be thought of as a coordinate transform, depending on the large-scale velocity features, that maps the reflection events in the data to focussed point sources at their respective reflectors. The radiation pattern of these point sources reveals the angle-dependent reflection coefficient and can be used to infer the local rock properties. Errors in the large-scale velocity features are revealed through the failure of the events to fully focus. This principle forms the basis of all velocity analysis procedures.

Over the past decades, various methods have been proposed for computing image volumes or slices thereof – the so-called image gathers. These approaches differ in the way the redundant coordinate is introduced and the method used to transform the data volume to an image volume. Perhaps the most well-known example is the midpoint gather, where a simple move-out correction transforms the data into a volume as a function of time, midpoint position and offset. The use of a one-way wave equation to produce an image volume as a function of depth and virtual subsurface source and receiver positions using the so-called *double-square-root equation* was proposed by Doherty and Claerbout (1974).

The use of subsurface offset, rather than surface offset, as redundant coordinate was justified by Stolk et al. (2009), who showed that this produces artifact-free image gathers in complex geological settings. The latest development along this line is the use of the two-way wave-equation to compute gathers as a function of depth and horizontal or vertical offset, or both (Biondi and Symes, 2004; Sava and Vasconcelos, 2011). This is achieved by forward propagating the source and backward propagating the data and subsequently correlating these source and receiver wave fields at non-zero lag. This leads to the notion of extended imaging conditions (Sava and Biondi, 2004; Sava and Fomel, 2006) that dictate how the multi-dimensional correlation is transformed into an image gather. The motivation to depart from horizontal offset only is that steeply dipping events do not optimally focus in the horizontal direction, even for a kinematically correct velocity model. A temporal shift instead of a subsurface offset is sometimes used as it is more computationally efficient MacKay and Abma (1992); Sava and Fomel (2006).

Each subsequent advancement in image-gather-based velocity-model building is due to a better sampling of the extended image and/or a more accurate wave propagator. As a result, one is inclined to declare that the ultimate goal of these approaches is to form an image volume as a function of *all* subsurface offsets and time-lags (or equivalently, frequencies) for *all* subsurface points using the two-way scalar wave-equation. Many practical implementations rely on initially computing the full source and receivers wavefields and subsequently cross-correlating them. To make such an approach computationally feasible, the permitted interaction between the wavefields is restricted, (e.g., by allowing only for lateral interaction over a short distance), and the gathers are computed for a few subsurface image points. Sava and Vasconcelos (2011) presents an analysis of the computational complexity of cross-correlating the given wavefields for various imaging conditions that not

only involve expensive correlations but also grow linearly in the number of sources which can be prohibitively expensive for even small two-dimensional problems.

One way of extracting a velocity update from these image gathers is by wave-equation migration velocity analysis (WEMVA). Here, we formulate an appropriate cost function to measure the coherency of the image gathers (Symes and Carazzone, 1991; Shen and Symes, 2008) and use a gradient-based method to find a velocity model that optimizes the objective function. Again, we can never hope to compute and store the complete image volume, much less solve an optimization problem that relies on repeatedly forming it. One of the solutions to making this process computationally feasibly is to severely subsample the extended image by restricting the allowed interaction and computing the gathers only at a few judiciously chosen points (Yang and Sava, 2015). Common features of all current workflows for wave-equation migration velocity analysis are that they *i)* compute all the source and receiver wavefields; *ii)* severely subsample the image volume in the subsurface coordinates and *iii)* allow for limited interaction of the wavefields in predefined directions according to the geological setting.

Amplitude-versus-angle (AVA) or Amplitude-versus-offset (AVO) inversion relies on matching the observed amplitudes of a certain event in the image volume to a model. The simplest model for this purpose are the linearized Zoepptriz equations (Aki and Richards, 1980). Extensive research has been done in this area where reliable angle-domain image gathers are produced with correct amplitude-versus-angle response in complex geological environments with variable angle-dips and in the presence of source and receivers ghosts (de Bruin et al., 1990; van Wijngaarden, 1998; Rickett and Sava, 2002; Sava and Fomel, 2003; Kuhel and Sacchi, 2003; Biondi and Symes, 2004; Sava and Vasconcelos, 2011; Bai et al., 2013). Recently, Lu et al. (2014b) showed that the multiple-only data can be used

to generate angle-domain image gathers to get good angular illumination in conventional marine towed-streamer acquisition.

The current workflows involving image volumes are pushing for better sampling of the image volume and more realistic physics. At the same time the computational costs involved restrict the number of samples than be computed, forcing practitioners to pre-select points of interest and geological dips before computing the image gathers. This prompted us to ask the following questions:

Can we devise a method that gleans information from the full image volume without requiring a-priori knowledge of the geology?

and,

If we are not forming the full image volume anyway, is it possible to avoid computing all of the wavefields?

In this paper, we propose a new perspective on extended images that can serve as the basis for a new generation of algorithms and workflows that incorporate extended images, such as AVA/AVO inversion and wave-equation migration velocity analysis. The basic idea is as follows; instead of severely subsampling the image volume –which may induce unwanted artifacts in the resulting image gathers– we propose to probe the full image volume for information by computing the action of the image volume on given vectors. We show that such actions can be computed cheaply, *without forming the source and receiver wavefields for all sources*, and demonstrate how they can be used to extract various traditional image gathers and formulate objective functions for automatic wave-equation migration velocity analysis.

The paper proceeds as follows. First, we express the extended image in terms of discrete

data-matrices and discuss how various conventional image gathers are embedded in this matrix. We then discuss the physics of underlying the extended image in the case of the full two-way wave equation and derive a two-way equivalent of the *double square-root equation*. We show how actions of the image-volume matrix on vectors can be computed and we present some applications, namely; the computation of local-geological dip information, the extraction of angle-gathers for arbitrary dip, amplitude-versus-angle analysis, and automatic migration velocity analysis. We use stylized numerical examples to illustrate the workings of the proposed methods. Finally, we present the discussion and conclusions.

ANATOMY

Before describing the proposed methodology of extracting information from the full extended image using probing techniques, we review the equations governing extended images. We denote the full extended image as

$$e(\omega, \mathbf{x}, \mathbf{x}') = \int_{\mathcal{D}_s} \mathrm{d}\mathbf{x}_s \; u(\omega, \mathbf{x}, \mathbf{x}_s)\overline{v(\omega, \mathbf{x}', \mathbf{x}_s)}, \tag{1}$$

where the overline denotes complex conjugation, u and v are the source and receiver wavefields as a function of the frequency $\omega \in \Omega \subset \mathbb{R}$, subsurface position $\mathbf{x}, \mathbf{x}' \in \mathcal{D} \subset \mathbb{R}^n$ ($n = 2$ or 3) and source position $\mathbf{x}_s \in \mathcal{D}_s \subset \mathbb{R}^{n-1}$. These wavefields are obtained by solving

$$H(m)u(\omega, \mathbf{x}, \mathbf{x}_s) \;=\; q(\omega, \mathbf{x}, \mathbf{x}_s), \tag{2}$$

$$H(m)^* v(\omega, \mathbf{x}, \mathbf{x}_s) \;=\; \int_{\mathcal{D}_r} \mathrm{d}\mathbf{x}_r \; d(\omega, \mathbf{x}_r, \mathbf{x}_s)\delta(\mathbf{x} - \mathbf{x}_r), \tag{3}$$

where $H(m) = \omega^2 m(\mathbf{x})^2 + \nabla^2$ is the Helmholtz operator with Sommerfeld boundary conditions, the symbol * represents the conjugate-transpose (adjoint), m is the squared slowness, q is the source function and d represents the observed data at receiver positions $\mathbf{x}_r \in \mathcal{D}_r \subset \mathbb{R}^{n-1}$.

Equations (1-3) define a linear mapping from the $2n-1$ dimensional data volume $d(\omega, \mathbf{x}_r, \mathbf{x}_s)$ to the $2n+1$ dimensional image volume $e(\omega, \mathbf{x}, \mathbf{x}')$. The conventional migrated image is obtained by applying an imaging condition

$$r(\mathbf{x}) = \int_\Omega \mathrm{d}\omega \; e(\omega, \mathbf{x}, \mathbf{x}). \tag{4}$$

In the remainder of the paper, we will restrict ourselves to the two-dimensional case ($n = 2$) for the purpose of illustration. The proposed methodology is completely generic, however, and is readily extended to $n = 3$.

Once we have the full extended image, we can extract all conceivable image and angle gathers by applying appropriate imaging conditions (Sava and Vasconcelos, 2011). A conventional common image gather (CIG), as a function of midpoint x_m, depth z and horizontal offset h_x, for example, is defined as

$$\mathbf{I}_{\mathrm{CIG}}(z, h; x_m) = \int_\Omega \mathrm{d}\omega \; e\left(\omega, (x_m - h_x, z)^T, (x_m + h_x, z)^T\right). \tag{5}$$

A common image point gather (CIP) at a point $\mathbf{x}_0$, as a function of all spatial offsets $\mathbf{h} = (h_x, h_z)^T$ and a temporal shift Δt is defined as

$$\mathbf{I}_{\mathrm{CIP}}(\mathbf{h}, \Delta t; \mathbf{x}_0) = \int_\Omega \mathrm{d}\omega \; e(\omega, \mathbf{x}_0, \mathbf{x}_0 + \mathbf{h}) e^{\imath\omega\Delta t}. \tag{6}$$

Here, h_z and the symbol ^{T} represent the vertical offset and transpose, respectively. Note that we depart from the usual symmetric definition $e(\omega, \mathbf{x}_0 - \mathbf{h}, \mathbf{x}_0 + \mathbf{h})$ because it turns out to be more natural for shot-based computations.

Moving to a discrete setting, we have N_s sources $\{\mathbf{x}_{s,i}\}_{i=1}^{N_s} \in \mathcal{D}_s$, N_r receivers $\{\mathbf{x}_{r,i}\}_{i=1}^{N_r} \in \mathcal{D}_r$, N_f frequencies $\{\omega_i\}_{i=1}^{N_f} \in \Omega$ and discretize the domain $\mathcal{D}$ using a rectangular grid with a total of N_x grid points $\{\mathbf{x}_i\}_{i=1}^{N_x}$. We organize the source and receiver wavefields in tensors of size $N_f \times N_x \times N_s$ with elements $u_{ijk} = u(\omega_i, \mathbf{x}_j, \mathbf{x}_{s,k})$ and $v_{ijk} = v(\omega_i, \mathbf{x}_j, \mathbf{x}_{s,k})$. For the

i^{th} frequency, we can represent the wavefields for all sources as $N_x \times N_s$ matrices $\mathbf{U}_i$ and $\mathbf{V}_i$, where each column of the matrix represents a monochromatic source experiment.

The full $2n+1$ dimensional image volume can now be represented as a 3-dimensional tensor with elements $e_{ijk} = e(\omega_i, \mathbf{x}_j, \mathbf{x}_k)$. A slice through this tensor at frequency i is an $N_x \times N_x$ matrix, which can be expressed as an outer product of the matrices $\mathbf{U}_i$ and $\mathbf{V}_i$

$$\mathbf{E}_i = \mathbf{U}_i \mathbf{V}_i^*, \tag{7}$$

where * denotes the complex conjugate transpose. The matrix $\mathbf{E}_i$ is akin to Berkhout's *reflectivity matrices* (Berkhout, 1993). The usual imaging condition translates to

$$\mathbf{r} = \sum_{i=1}^{N_f} \text{diag}(\mathbf{E}_i), \tag{8}$$

where $\mathsf{diag}(\mathbf{A})$ denotes the diagonal elements of $\mathbf{A}$ organized in a vector. Various image gathers are embedded in this matrix as illustrated in Figure 1.

As we will switch between continuous and discrete notation throughout the paper, the correspondence between the image volume $e(\omega, \mathbf{x}, \mathbf{x})$ and the matrices $\mathbf{E}_i$ is listed in Table 1. We will drop the frequency-dependence from the notation in the remainder of the paper and implicitly assume that all quantities are monochromatic with the understanding that all computations can be repeated as needed for multiple frequencies.

PHYSICS

We consider using the two-way wave-equation to obtain the source and receiver wavefields, in which case the source and receiver wavefields satisfy

$$\mathbf{H}(\mathbf{m})\mathbf{U} = \mathbf{P}_s^*\mathbf{Q}, \tag{9}$$

$$\mathbf{H}(\mathbf{m})^*\mathbf{V} = \mathbf{P}_r^*\mathbf{D}, \tag{10}$$

where $\mathbf{H}(\mathbf{m})$ is a discretization of the Helmholtz operator with absorbing boundary conditions for gridded squared slowness $\mathbf{m}$, the $N_s \times N_s$ matrix $\mathbf{Q}$ represents the sources (i.e., each column is a source function), the $N_r \times N_s$ matrix $\mathbf{D}$ contains pre-processed data (i.e., each column is a monochromatic shot-gather) and the matrices $\mathbf{P}_s, \mathbf{P}_r$ sample the wavefield at the source and receiver positions (and hence, their transpose injects the sources and receivers into the grid). In practise, this pre-processing typically entails removal of the direct-wave and surface-related multiples. Substituting relations (9), (10) into the definition of the extended image (7) yields

$$\mathbf{HEH} \;=\; \mathbf{P}_s^* \mathbf{Q} \mathbf{D}^* \mathbf{P}_r, \tag{11}$$

which is a discretization of the following *double* wave-equation

$$\begin{aligned} &\left[\omega^2 m(\mathbf{x}) + \nabla^2_{\mathbf{x}}\right] \left[\omega^2 m(\mathbf{x}') + \nabla^2_{\mathbf{x}'}\right] e(\omega, \mathbf{x}, \mathbf{x}') \\ &\quad = \int_{\mathcal{D}_s} \mathrm{d}\mathbf{x}_s \int_{\mathcal{D}_r} \mathrm{d}\mathbf{x}_r \; d(\omega, \mathbf{x}_s, \mathbf{x}_r) q(\omega, \mathbf{x}_s) \delta(\mathbf{x} - \mathbf{x}_s) \delta(\mathbf{x}' - \mathbf{x}_r). \end{aligned} \tag{12}$$

Equation (12) can be seen as a generalization of the double square-root (DSR) equation, which uses a one-way approximation and allows for lateral interaction only.

From equation (11) we derive the following expression of the image volume

$$\mathbf{E} \;=\; \mathbf{H}^{-1} \mathbf{P}_s^* \mathbf{Q} \mathbf{D}^* \mathbf{P}_r \mathbf{H}^{-1}, \tag{13}$$

which is a discrete analogue of the mapping from the data to the image volume defined in equations (1-3). Note that for co-located sources and receivers ($\mathbf{P}_r = \mathbf{P}_s$) and ideal point sources ($\mathbf{Q}$ is the identity matrix) we find that $\mathbf{E}$ is complex symmetric (i.e., $\Re(\mathbf{E}^*) = \Re(\mathbf{E})$ and $\Im(\mathbf{E}^*) = -\Im(\mathbf{E})$) because of source-receiver reciprocity.

COMPUTATION

Of course, we can never hope to explicitly form the whole image volume owing to the enormous computational and storage costs: computing the full image matrix requires $2N_s$ wave-equation solves and the storage of a dense $N_x \times N_x$ matrix. Instead of computing the full matrix $\mathbf{E}$, we propose to subsample it by multiplying it with a given $N_x \times L$ sampling matrix with probing vectors $\mathbf{W} = [\mathbf{w}_1, \ldots, \mathbf{w}_L]$, which we can express as

$$\widetilde{\mathbf{E}} = \mathbf{E}\mathbf{W} = \mathbf{H}^{-1}\mathbf{P}_s^*\mathbf{Q}\mathbf{D}^*\mathbf{P}_r\mathbf{H}^{-1}\mathbf{W}, \tag{14}$$

where $L < N_s$ denotes the number of samples. We can compute this product efficiently as follows:

1. compute $\widetilde{\mathbf{U}} = \mathbf{H}^{-1}\mathbf{W}$ and sample this wavefield at the receiver locations $\widetilde{\mathbf{D}} = \mathbf{P}_r\widetilde{\mathbf{U}}$;
2. correlate the result with the data $\widetilde{\mathbf{W}} = \mathbf{D}^*\widetilde{\mathbf{D}}$ to get the source weights;
3. use the source weights to generate the simultanoues sources $\widetilde{\mathbf{Q}} = \mathbf{Q}\widetilde{\mathbf{W}}$;
4. compute the resulting wavefields $\widetilde{\mathbf{E}} = \mathbf{H}^{-1}\mathbf{P}_s^*\widetilde{\mathbf{Q}}$.

The computational cost of this algorithm is $2L$ wave-equation solves plus the cost of auto-correlating the data matrix.

Using the above mentioned procedure, we can form a so-called common-image point gather $e(\omega, \mathbf{x}_i, \mathbf{x})$, centered around $\mathbf{x}_i$, as a function of *all* subsurface offsets by having the probing vector $\mathbf{w}_i$ represent a point source at location $\mathbf{x}_i$. For comparison, the conventional way to compute such common-image point is as follows:

1. compute all the source wavefields $\mathbf{U} = \mathbf{H}^{-1}\mathbf{P}_s^*\mathbf{Q}$,

2. compute all the receiver wavefields $\mathbf{V} = \mathbf{H}^{-*}\mathbf{P}_r^*\mathbf{D}$

3. select the i^{th} row from the receiver wavefield matrix, i.e.,$\mathbf{w}_i = \mathbf{V}_{i,:}$

4. compute the product $\widetilde{\mathbf{E}} = \mathbf{U}\mathbf{w}_i^*$.

Table 2 summarizes the computational complexity of the two schemes in terms of the number of sources N_{s}, receivers N_{r} sample points N_x and desired number of subsurface offsets in each direction $N_{h_{\{x,y,z\}}}$. To illustrate the benefits of the proposed scheme, we also report the computational time (in sec) and memory (in MB) required to compute a single common-image point gather for a 2D synthetic (1-layer) model of 51×101 gridpoints, using 25 frequencies and 51 sources and receivers. The results are shown in Table 3. We can see that even for a small toy model, the probing technique reduces the computational time and memory requirements by a factor of 10 and 30, respectively. In the following sections, we discuss a number of applications of these image volumes and how we can use the aforementioned probing technique in each application to implement a computationally efficient algorithm.

DIP-ANGLE GATHERS

Angle-domain common-image gathers can be used to study the amplitude-versus-angle behaviour of certain reflectors, and ultimately to invert for rock properties (Mahmoudian and Margrave, 2009). For this purpose, various definitions of angle-domain common-image gathers have been proposed (de Bruin et al., 1990; van Wijngaarden, 1998; Rickett and Sava, 2002; Sava and Fomel, 2003; Kuhel and Sacchi, 2003; Biondi and Symes, 2004; Sava and Vasconcelos, 2011). Following de Bruin et al. (1990), we extract the angle dependent

reflection coefficient from a scatterer at location $\mathbf{x}$ with dip θ as

$$R(\alpha;\mathbf{x},\theta)=\int_{\Omega}\mathrm{d}\omega\int_{-h_{\max}}^{h_{\max}}\mathrm{d}h\ \ e(\omega,\mathbf{x},\mathbf{x}+h\mathbf{n}(\theta)^{\perp})e^{\imath\omega\sin(\alpha)h/v}, \tag{15}$$

where α is the angle of incidence with respect to the normal vector of the reflector $\mathbf{n}(\theta)=(\sin\theta,\cos\theta)^T$, $\imath=\sqrt{-1}$, v is the local velocity, $\mathbf{n}(\theta)^{\perp}$ denotes the tangent of the reflector and $h_{\max}$ denotes the maximal subsurface offset. A schematic depiction of the situation is shown in figure 2.

An angle gather, as a function of depth and angle, can now be constructed by densely sampling R at locations $\{\mathbf{x}_i\}$ along the z-axis. To estimate the geological dip at the reflectors, we use a stack-power approach. First, we define a stack power

$$S(\theta;\mathbf{x}_i)=\int_{-h_{\max}}^{h_{\max}}\mathrm{d}h\ \ \left|\int_{\Omega}\mathrm{d}\omega\ e(\omega,\mathbf{x}_i,\mathbf{x}_i+h\mathbf{n}(\theta))\right|^2. \tag{16}$$

which stacks the extended image in the direction normal to a reflector with dip θ. We expect that this stack assumes a maximum at the true dip (Brandsberg-Dahl et al., 2003).

To compute the angle-dependent reflection coefficient at a given location $\mathbf{x}_i$, we first compute the common-image point around $\mathbf{x}_i$ by multiplying the matrix $\mathbf{E}$ with a vector $\mathbf{w}_i$ that represents a point source at $\mathbf{x}_i$. The resulting gather $e(\omega,\mathbf{x}_i,\mathbf{x})$ contains all the information needed to compute both the reflection coefficient and the stackpower for *arbitary* angle and dip. Thus, estimation of the dip can be performed by maximizing the stack power at no significant additional computational cost. Having obtained the optimal dip θ_i that maximizes $S(\theta,\mathbf{x}_i)$, we can compute the angle-dependent reflectivity $R(\alpha;\mathbf{x}_i,\theta_i)$.

Numerical results

To illustrate the proposed method of computing angle-domain common-image gathers, we compare the modulus of the reflection coefficient $|R(\alpha; \mathbf{x}_i, \theta_i)|$ with the theoretical reflection coefficients as predicted by the (linearized) Zoeppritz equations (Koefoed, 1955; Shuey, 1985). We use a finite difference time-domain code (Symes et al., 2011) to generate the synthetic data sets for three variable density models: the first model consists of one layer with constant density (Figure 3(a)), the second model has four layers with the same medium properties as described in de Bruin et al. (1990) (Figure 4(a,b)), and the third model has two layers, one-horizontal reflector and one-dipping reflector (Figure 6(a)). The source signature is a Ricker wavelet with a peak frequency of 15 Hz.

The reflection coefficients for the first model are displayed in Figure 3(b). We can see that the extracted reflection coefficient matches very well with the theoretical results. The results on the four-layer model are displayed in Figure 4. We can see that the reflection coefficients for the first and second reflector are well matched up to 50° and 40° and, for the third and fourth reflectors, are well matched up to 20°. The finite aperture of the data accounts for the discrepancy beyond these angles. Finally, we perform the reflectivity analysis on the third model (Figure 5(c)), where we also estimate the local dip using the stack-power approach. We can see in Figure 5(c) that the common-image point gather is fully focused and aligned with the local dip. Figure 5(d) shows that the maximum stack-power corresponds to a dip-angle of 10.6°. To show the effect of the geological dip on the angle gathers, we compute the angle-dependent reflectivity coefficients with a wrong dip ($\theta = 0°$) and with the dip obtained via the stack-power method described previously ($\theta \approx 10.6°$). The results are depicted in figure 6. We can clearly see the benefit of incorporating the

dip-information in angle-domain image gathers as it allows for a more accurate estimation of the angle-dependent reflection coefficients. The experimental result shows the efficacy of stack-power method to accurately estimate the geological dip value.

DIFFERENTIAL SEMBLANCE

Wave-equation migration velocity analysis is another important application where image gathers have been studied extensively. The aim of wave-equation migration velocity analysis is to build a kinematically accurate velocity model by finding a velocity model that focusses a set of image gathers. One way of finding such a model is through *Differential semblance*. The basic idea is to minimize a suitable cost function that measures the focussing of the image gathers (Shen and Symes, 2008; Symes, 2008b). To account for varying (and unknown) geological dips Sava and Vasconcelos (2011); Yang and Sava (2015) propose to use *all* subsurface offsets and time-lags to formulate such an objective for a pre-selected set of subsurface points. In terms of the extended image volume, we can formulate this method as

$$\min_{\mathbf{m}} \sum_{i=1}^{K} \|\mathbf{S}_i \mathbf{E}(\mathbf{m}) \mathbf{p}_i\|_2^2, \tag{17}$$

where $\mathbf{E}(\mathbf{m})$ denotes the extended image volume for velocity model $\mathbf{m}$, $\mathbf{p}_i$ represents a point-source at midpoint $\mathbf{x}_i$ and $\mathbf{S}_i$ denotes a weight that penalizes defocused events. The main computational cost of solving equation (17) lies in computing the gathers for each midpoint.

An alternative formulation is based on the observation that, for a kinematically correct velocity model, the extended image matrix commutes with multiplication by diagonal matrix

[1]:

$$\mathbf{E}\text{diag}(\mathbf{s}) \approx \text{diag}(\mathbf{s})\mathbf{E}, \tag{18}$$

where $\mathbf{s}$ is a given vector. An intuitive explanation is that we expect $\mathbf{E}$ to be nearly diagonal for a kinematically correct model, so that it commutes with a diagonal matrix. If we choose the entries of $\mathbf{s}$ to correspond to the lateral coordinate of each gridpoint, this formulation is actually equivalent to the conventional differential semblance formulation that penalizes defocussing in the lateral direction (Symes, 2014). The corresponding optimization problem is given by

$$\min_{\mathbf{m}} \left\{ \phi(\mathbf{m}) = ||\mathbf{E}(\mathbf{m})\text{diag}(\mathbf{s}) - \text{diag}(\mathbf{s})\mathbf{E}(\mathbf{m})||_F^2 \right\}, \tag{19}$$

where $||\mathbf{A}||_F^2 = \sum_{i,j} a_{i,j}^2$ denotes the Frobenius norm. Computationally, this is not a practical program to solve since, even in 2D, it is prohibitively expensive to recompute and store the extended image for all the subsurface points at each iteration of an optimization algorithm. However, we can efficiently approximate the objective function in equation (19) by using only a few matrix-vector products with $\mathbf{E}$ as

$$\phi(\mathbf{m}) \approx \widetilde{\phi}(\mathbf{m}) = \frac{1}{K} \sum_{i=1}^{K} \|\mathbf{R}(\mathbf{m})\mathbf{w}_i\|_2^2, \tag{20}$$

where $\mathbf{R}(\mathbf{m}) = \mathbf{E}(\mathbf{m})\text{diag}(\mathbf{s}) - \text{diag}(\mathbf{s})\mathbf{E}(\mathbf{m})$ and $\mathbf{w}_i$ are i.i.d. random vectors with zero mean and unit variance (Avron and Toledo, 2011). The dominant computational cost of evaluating $\phi(\mathbf{m})$ is $2N_s$ wave-equation solves, whereas an evaluation of $\widetilde{\phi}(\mathbf{m})$ requires $2K$ wave-equation solves. This approximation is akin to the source-encoding techniques used in full-waveform inversion and experience suggests that we can choose K to be much smaller than N_s (Krebs et al., 2009; van Leeuwen et al., 2011; Haber et al., 2012). In the current context, we can interpret the random vectors as simultaneous subsurface sources.

[1] W.W. Symes, personal communication

The gradient of the proposed objective is given by

$$\nabla\widetilde{\phi}(\mathbf{m}) = \frac{1}{K}\sum_{i=1}^{K}\big(\nabla\mathbf{E}(\mathbf{m},\mathrm{diag}(\mathbf{s})\mathbf{w}_i) - \mathrm{diag}(\mathbf{s})\nabla\mathbf{E}(\mathbf{m},\mathbf{w}_i)\big)^*\mathbf{R}(\mathbf{m})\mathbf{w}_i, \tag{21}$$

where

$$\nabla\mathbf{E}(\mathbf{m},\mathbf{y}) = \frac{\partial\mathbf{E}(\mathbf{m})\mathbf{y}}{\partial\mathbf{m}}$$

is the Jacobian of $\mathbf{E}(\mathbf{m})\mathbf{y}$. Of course we do not form this Jacobian matrix explicitly, but instead compute its action on a vector as follows

$$\nabla\mathbf{E}(\mathbf{m},\mathbf{y})\delta\mathbf{m} \quad = \quad -\omega^2\left(\mathbf{E}(\mathbf{m})\mathrm{diag}(\widetilde{\mathbf{y}}) + \mathbf{H}(\mathbf{m})^{-1}\mathrm{diag}(\widetilde{\mathbf{e}})\right)\delta\mathbf{m} \tag{22}$$

where $\widetilde{\mathbf{w}} = \mathbf{H}(\mathbf{m})^{-1}\mathbf{y}$, $\widetilde{\mathbf{e}} = \mathbf{E}(\mathbf{m})\mathbf{y}$. The computation of the action of the adjoint of the Jacobian follows naturally.

It can be shown that the objective $\widetilde{\phi}$ and its gradient are *unbiased* approximations of the full objective ϕ and its gradient (van Leeuwen et al., 2011; Haber et al., 2012). We can now employ any iterative gradient-based method to find a minimizer of $\phi(\mathbf{m})$ using the stochastic approximations stated above. In practice, the random vectors $\mathbf{w}_i$ are not fixed but are re-drawn at each iteration to remove the possible bias introduced by using fixed set of vectors. Convergence may further be improved by gradually increasing the number of samples K. The theoretical underpinning for such approaches comes from the field of *stochastic optimization* (Haber et al., 2012; Friedlander and Schmidt, 2012).

Experiments and results

We test the proposed wave-equation migration velocity analysis formulation on synthetic examples, showing the efficacy of the probing techniques along with the usefulness of full subsurface image volumes.

Our first experiment demonstrate the benefit of working with all the subsurface offsets. Figure 7 (a) shows a synthetic velocity model that has both a horizontal and a vertical reflector. The reason of working with this particular velocity model is to show the sensitivity of the common-image point gathers to the different geological dips (in this case two extreme dip values i.e. 0° and 90°) present in the model. To show the benefits of common-image points over common-image gathers, we construct the common-image gathers along the yellow line and common-image point gathers centered around the green dots, as outlined in the figure using the kinematically correct velocity model. We expect to get focused common-image gather and common-image point gather for this velocity model. In Figure 7, we show the image gathers corresponding to the vertical and horizontal reflector in the top and bottom rows, respectively, as a function of vertical offset (b,e), horizontal offset (c,f) and both horizontal and vertical offsets (d,g). While the common-image gathers (b,c,e,f) only focus if the offset is aligned with the local dip, the common-image point gathers (d,g) do not assume a geological dip and focus around zero offset. Therefore, when considering a complex geological model with very steep structures, working with common-image points helps to analyze the focusing of reflectors with arbitrary dips, hence removing any directional bias in performing wave-equation based migration velocity analysis on a subsurface structure.

The next experiment shows the effectiveness of the stochastic approximation of the objective function. For this purpose, we consider a subset of the marmousi model as depicted in Figure 8 (a). Figure 8 (b) shows $\phi(\mathbf{m}_0+\alpha\delta\mathbf{m})$ and $\tilde{\phi}(\mathbf{m}_0+\alpha\delta\mathbf{m})$ as a function of α where we choose $\delta\mathbf{m} = -\nabla\phi$ and $\mathbf{m}_0$. We take $\mathbf{w}_i$ to be i.i.d. Gaussian random vectors with mean zero and unit variance. The results using $K = 10$ and 80 are shown in figure 8 (c,d). The error bars indicate the maximum deviation over 5 independent random realizations. These

results show that we can substantially reduce the computational costs while approximating the true objective function accurately.

Finally, we test the effectiveness of the proposed wave-equation migration velocity analysis formulation on two different velocity models. To regularize the inversion and impose the smoothness on the gradient, we parameterize the model using cubic B-splines (Symes, 2008a). We solve the resulting optimization problem using a limited-memory Broyden-Fletcher-Goldfarb-Shanno (L-BFGS) method (Nocedal and Wright, 2000). The first example represents a high velocity anomaly embedded in a 1D horizontally layered model. The model is 1.8 km deep and 3 km wide, sampled at 20 m intervals, respectively. Sources and receivers are placed at the surface with a sampling interval of 20m. We use 25 frequencies ranging from 3 to 15 Hz. We choose $K = 100$ and performed 30 L-BFGS iterations. Figures 9 (a,e) show the corresponding true velocity model and the image gather. The initial model, shown in Figure 9b, is far from the true model as reflected in the defocused image gathers, shown in Figure 9 (f). Figures 9 (c,g) depict the estimated velocity model and the corresponding image gathers. These show that our method successfully focusses the gathers and reconstructs the anomaly. This is further verified by inspecting the least-squares migrated images for the true, initial and final models (Figures 10). Whereas the reflectors are curved for the initial model, they are mostly flattened in the final model.

The second example, shown in Figure 11 (a), represents a more complex model with steeply dipping reflectors. We placed sources and receivers at the surface with spacing of 20 m and a total of 41 frequencies are used, ranging from 3 to 15 Hz. We choose $K = 200$ and the sampling interval of the B-splines is 48 m. The initial velocity model, shown in Figure 11 (b), is a highly smoothed version of the true model. Figure 11 (c) shows the inverted model using the proposed formulation after 4 L-BFGS iterations. The image gathers for the

true, initial and inverted models, respectively are shown in Figure 11 (d-f). We can see that events are well-focused and at the correct position up to the depth of 1.2 km. We do not expect good results beyond this due to the limited aperture. The overlay of the true model perturbation and the inversion result (Figure 12) shows that the structure in the velocity model corresponds to the true geological structure.

DISCUSSION

The matrix-view of the extended image volume offers a new perspective on the design and implementation of workflows that exploit the information embedded in various types of extended images. The current paper presents a proof-of-concept and illustrates the merit of the matrix-viewpoint. The use of probing techniques for image volumes is closely related to the use of simultaneous-source techniques of full-waveform inversion. Since both techniques derive from the same principles of stochastic optimization, therefore, we expect them to work well and lead to enabling improvements in computational efficiency. Indeed, the output of a matrix-vector multiplication of the image volume with a random vector can be seen as the result of a simultaneous subsurface source experiment. The trace-estimation technique discussed to approximate the objective function for velocity analysis is closely related to an emerging class of *matrix sketching* methods that aim to estimate properties of exceedingly large matrices (Woodruff, 2014). Results from this field can be used to obtain better estimators of other properties of the misfit function of large extended image volumes besides the trace, and derive bounds on the number of probing vectors required to guarantee a certain accuracy. The challenge will be to incorporate the detailed knowledge of the underlying physics of the image volumes in the theoretical framework that largely deals with random matrices.

Future directions

One of the current limitations of working with image gathers is that the extended imaging conditions cannot handle primary and multiple reflections simultaneously. Multiples, especially the surface-related multiples, form a significant part of the total up-going wavefield. If not properly dealt with, they can lead to ghost reflectors in the image gathers which focus at the wrong velocity. Therefore, practitioners remove them prior to migration (Verschuur, 2006). However, multiples can actually provide extra illumination and are more sensitive to velocity changes (Verschuur, 1991, 2006, 2011; Tu et al., 2013). An obvious way of incorporating multiples is to separate the data into primaries and multiples first, and form separate (extended) images from them (Lu et al., 2014a). However, the separation of primary and multiple wavefields is challenging, computationally expensive, and may damage the primary signal. Therefore, Kumar et al. (2015) proposed to use primaries and multiples simultaneously when forming image gathers. The preliminary results showed a promising approach where multiples are incorporated directly in least-squares extended imaging by simply replacing the source terms by the total down-going wavefield, as demonstrated by Tu et al. (2013) for least-squares reverse-time migration.

The proposed wave-equation based migration velocity analysis formulation is based on a single-scattering assumption. Liu et al. (2014b) showed that this can lead to undesired artifacts in the extended images. The cause of these artifacts is the failure of the Born scattering operator to fully fit the observed data, even if the data contain only primary events. Some approximate inversion approaches have recently been proposed to eliminate these artifacts (Lameloise et al., 2014). The ultimate goal, however, is to obtain the extended images itself via a non-linear data-fitting procedure in line with full-waveform inversion

(Symes, 2008c). Some very promising work in this direction was recently presented by Biondi & Almomin (Biondi and Almomin, 2013; Almomin and Biondi, 2014) and Symes et al. (Sun and Symes, 2013; Liu et al., 2014a). The matrix-probing ideas presented in this paper can be directly incorporated in these existing approaches. The matrix interpretation of the extended image, however, may also lead to a completely new formulation of the fully non-linear problem (Symes, 2008c).

Another exciting prospect is the extension of the matrix viewpoint to the elastic case. In this case, the monochromatic extended image matrix would become a tensor that additionally captures the interaction between different wave modes. The advantage of imaging with different wave modes (primary and shear modes) is that the physics of wave propagation is better represented, which allow us to make full use of information provided by elastic data and correctly position geologic structures. Yan and Sava (2008) presented a method for angle-domain extended imaging for multicomponent elastic data where elastic wavefields from the source and receivers were separated into pure compressional and transverse wave-modes which were then used to form angle-domain image gathers.

CONCLUSION

We present a alternative perspective on extended images based on a matrix representation of the image volume. Here, the extended image for a single frequency is organized as a matrix whose $(i,j)^{\text{th}}$ entry captures the interaction between subsurface gridpoints i and j. All conventional image gathers can be extracted from this matrix. Since it is infeasible to form and store the full extended image volume, we introduce an efficient way of gleaning information from this matrix by computing its action on input vectors. The dominant computational cost of one matrix-vector product is two wave-equation solves and does

not depend on the desired sampling of the subsurface offsets nor the number of sources and receivers. The proposed approach additionally avoids storing all the wavefields and thus reduces the memory requirements as well as compared to conventional approaches to computing the extended images.

We show that we can use the matrix-vector products to extract various image gathers at any desired subsurface position and how they can be used to perform amplitude-versus-angle analysis. An important step here is the estimation of the local geological dip. As the extracted image gathers contain all subsurface offsets by construction, we can easily estimate the geological dip by maximizing the stack-power. We test the proposed method on synthetic examples, showing that is possible to match the theoretical reflection coefficients when the dip is assumed unknown a-priori.

We also propose an alternative formulation of automatic wave-equation based migration velocity analysis. Traditionally, such formulations entail minimizing a weighted norm of the image gathers evaluated at pre-selected subsurface points. We formulate an equivalent problem that measures how well the total image volume (as a matrix) commutes with multiplication by a diagonal matrix. We then propose an algorithm that effectively tests this commutation relation on a set of randomly chosen input vectors. These probing vectors are effectively subsurface simultaneous sources and capture the focussing of the whole image volume, instead of just the focussing in a few preselected points. We demonstrate that only a few of these probing vectors suffice to approximate the true objective function, which measures the focussing in all subsurface points independently. We show, on synthetic examples, that by iteratively minimizing the proposed objective function we can obtain a kinematically correct model, even in the presence of strong lateral velocity variation and steeply dipping reflectors.

ACKNOWLEDGEMENTS

This work was in part financially supported by the NSERC and the Collaborative Research and Development Grant DNOISE II (375142-08).This research was carried out as part of the SINBAD II project with support from the following organizations: BG Group, BGP, Chevron, ConocoPhillips, DownUnder GeoSolutions, Hess, Petrobras, PGS, Woodside, CGG, Sub-Salt Solutions, and WesternGeco.

REFERENCES

Aki, K., and P. G. Richards, 1980, Quantitative seismology: Freeman and Co. New York, **1**.

Almomin, A., and B. Biondi, 2014, Preconditioned tomographic full waveform inversion by wavelength continuation: 84th SEG meeting, Denver, USA, Expanded Abstracts, P944–P948.

Avron, H., and S. Toledo, 2011, Randomized algorithms for estimating the trace of an implicit symmetric positive semi-definite matrix: Journal of the Association for Computing Machinery, **58**, P1–P16.

Bai, B., C. Chen, M. Yang, P. Wang, and Y. Huang, 2013, Ghost effect analysis and bootstrap deghosting application on marine streamer data: 75th EAGE, London, United Kingdom, Expended Abstracts.

Berkhout, A. J., 1993, A unified approach to acoustical reflection imaging. I: The forward model: The Journal of the Acoustical Society of America, **93**, 2005–2016.

Biondi, B., and A. Almomin, 2013, Tomographic full waveform inversion (TFWI) by extending the velocity model along the time-lag axis: 83rd SEG, Houston, Texas, USA, Expended Abstracts, 1031–1036.

Biondi, B., and W. W. Symes, 2004, Angle-domain common-image gathers for migration velocity analysis by wavefield-continuation imaging: Geophysics, **(5), 69**, 1283.

Brandsberg-Dahl, S., M. de Hoop, and B. Ursin, 2003, Focusing in dip and ava compensation on scattering angle/azimuth common image gathers: Geophysics, **(1), 68**, 232–254.

de Bruin, C., C. Wapenaar, and A. Berkhout, 1990, Angle-dependent reflectivity by means of prestack migration: Geophysics, **(9), 55**, 1223.

Doherty, S. M., and J. F. Claerbout, 1974, Velocity analysis based on the wave equation.:

Technical Report 1, Stanford Exploration Project.

Friedlander, M. P., and M. Schmidt, 2012, Hybrid Deterministic-Stochastic Methods for Data Fitting: SIAM Journal on Scientific Computing, **34**, A1380–A1405.

Haber, E., M. Chung, and F. Herrmann, 2012, An effective method for parameter estimation with pde constraints with multiple right-hand sides: SIAM Journal on Optimization, **22**, 739–757.

Koefoed, O., 1955, On the effect of poisson's ratios of rock strata on the reflection coefficients of plane waves: Geophysical Prospecting, **3**, 381–387.

Krebs, J., J. Anderson, D. Hinkley, R. Neelamani, S. Lee, A. Baumstein, and M. Lacasse, 2009, Fast full-wavefield seismic inversion using encoded sources: Geophysics, **(6), 74**, P177–P188.

Kuhel, H., and M. Sacchi, 2003, Least-squares wave-equation migration for avp/ava inversion: Geophysics, **(1), 68**, 262–273.

Kumar, R., N. Tu, T. van Leeuwen, and F. J. Herrmann, 2015, Least-squares extended imaging with surface-related multiples: GeoConvention, CSEG, Calgary, Canada.

Lameloise, C.-A., H. Chauris, and M. Noble, 2014, Improving the gradient of the image-domain objective function using quantitative migration for a more robust migration velocity analysis: Geophysical Prospecting.

Liu, Y., W. W. Symes, and Z. Li, 2014a, Extended Reflection Waveform Inversion via Differential Semblance Optimization: 84th SEG, Denver, USA, Expended Asbtracts.

———, 2014b, Inversion velocity analysis via differential semblance optimization: 76th EAGE, Amsterdam, The Netherlands, Expended Abstracts.

Lu, S., D. Whitmore, A. Valenciano, and N. Chemingui, 2014a, Enhanced subsurface illumination from separated wavefield imaging: First Break, **32**, 87–92.

Lu, S., N. Whitmore, A. Valenciano, and N. Chemingui, 2014b, Illumination from 3d imaging of multiples: An analysis in the angle domain: 84th SEG, Denver, USA, Expended Abstracts.

MacKay, S., and R. Abma, 1992, Imaging and velocity analysis with depth-focusing analysis: Geophysics, **(12), 57**, 1608–1622.

Mahmoudian, F., and G. F. Margrave, 2009, A review of angle domain common image gathers: Technical Report, University of Calgary.

Nocedal, J., and S. J. Wright, 2000, Numerical Optimization: Springer.

Rickett, J., and P. Sava, 2002, Offset and angle domain common imagepoint gathers for shot profile migration: Geophysics, **(3), 67**, 883–889.

Sava, P., and S. Fomel, 2003, Angle-domain common-image gathers by wavefield continuation methods: Geophysics, **(3), 68**, 1065–1074.

Sava, P., and I. Vasconcelos, 2011, Extended imaging conditions for wave-equation migration: Geophysical Prospecting, **59**, 35–55.

Sava, P. C., and B. Biondi, 2004, Wave-equation migration velocity analysis. I. Theory: Geophysical Prospecting, **52**, 593–606.

Sava, P. C., and S. Fomel, 2006, Time-shift imaging condition in seismic migration: Geophysics, **(6), 71**, S209—-S217.

Shen, P., and W. W. Symes, 2008, Automatic velocity analysis via shot profile migration: Geophysics, **(5), 73**, VE49–VE59.

Shuey, R., 1985, A simplification of the zoeppritz equations: Geophysics, **(4), 50**, 609–614.

Stolk, C. C., M. V. de Hoop, and W. W. Symes, 2009, Kinematics of shot-geophone migration: Geophysics, **(6), 74**, WCA19—-WCA34.

Sun, D., and W. Symes, 2013, Waveform Inversion via Nonlinear Differential Semblance

Optimization: 75th EAGE, London, united Kingdom, Workshop.

Symes, W., 2008a, Approximate linearized inversion by optimal scaling of prestack depth migration: Geophysics, **(2), 73**, R23–R35.

———, 2014, Seismic inverse poblems : recent developments in theory and practice: Proceedings of the Inverse Problems from Theory to Applications Conference, IOP Publishing, 2–6.

Symes, W. W., 2008b, Migration velocity analysis and waveform inversion: Geophysical Prospecting, **56**, 765–790.

———, 2008c, Migration velocity analysis and waveform inversion: Geophysical Prospecting, **56**, 765–790.

Symes, W. W., and J. J. Carazzone, 1991, Velocity inversion by differential semblance optimization: Geophysics, **(5), 56**, 654–663.

Symes, W. W., D. Sun, and M. Enriquez, 2011, From modelling to inversion: designing a well-adapted simulator: Geophysical Prospecting, **59**, 814–833.

Tu, N., A. Y. Aravkin, T. van Leeuwen, and F. J. Herrmann, 2013, Fast least-squares migration with multiples and source estimation: 75th EAGE, London, United Kingdom, Expended Abstracts.

van Leeuwen, T., A. Y. Aravkin, and F. J. Herrmann, 2011, Seismic waveform inversion by stochastic optimization: International Journal of Geophysics, **2011**.

van Wijngaarden, A., 1998, Imaging and characterization of angle-dependent seismic reflection data: PhD thesis, Delft University of Technology.

Verschuur, D. J., 1991, Surface-related multiple elimination, an inverse approach: PhD thesis, Delft University of Technology.

———, 2006, Seismic multiple removal techniques: Past, present and future: EAGE Course.

———, 2011, Seismic migration of blended shot records with surface-related multiple scattering: Geophysics, **(1), 76**, A7–A13.

Woodruff, D. P., 2014, Computational Advertising: Techniques for Targeting Relevant Ads: Foundations and Trends in Theoretical Computer Science, **10**, 1–157.

Yan, J., and P. Sava, 2008, Isotropic angle-domain elastic reverse-time migration: Geophysics, **(6), 73**, S229–S239.

Yang, T., and P. Sava, 2015, Image-domain wavefield tomography with extended common-image-point gathers: Geophysical Prospecting.

[Table 1 about here.]

[Table 2 about here.]

[Table 3 about here.]

[Figure 1 about here.]

[Figure 2 about here.]

[Figure 3 about here.]

[Figure 4 about here.]

[Figure 5 about here.]

[Figure 6 about here.]

[Figure 7 about here.]

[Figure 8 about here.]

[Figure 9 about here.]

[Figure 10 about here.]

[Figure 11 about here.]

[Figure 12 about here.]

LIST OF FIGURES

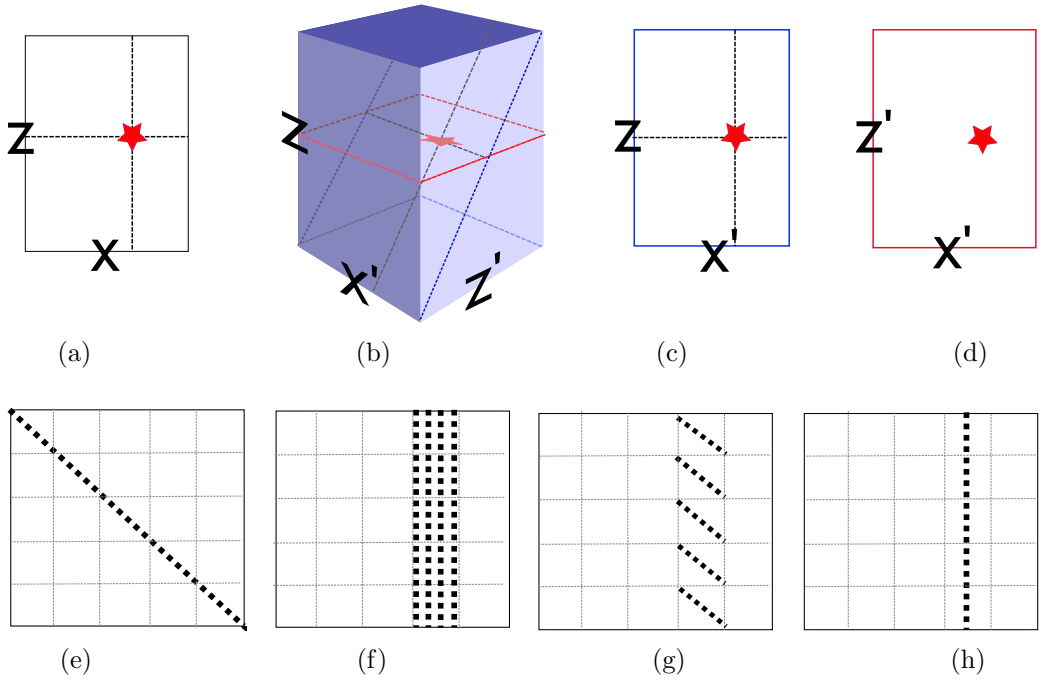

Figure 1: Different slices through the 4-dimensional image volume $e(z, z', x, x')$ around $z = z_0$ and $x = x_0$. (a) Conventional image $e(z, z, x, x)$, (b) Image gather for horizontal and vertical offset $e(z, z', x_0, x')$, (c) Image gather for horizontal offset $e(z, z, x_0, x')$ and (d) Image gather for a single scattering point $e(z_0, z', x_0, x')$. (e-g) shows how these slices are organized in the matrix representation of e.

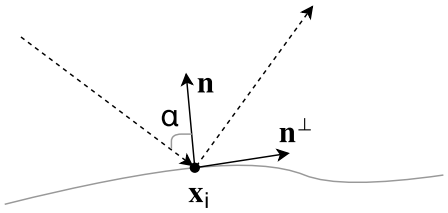

Figure 2: Schematic depiction of the scattering point and related positioning of the reflector.

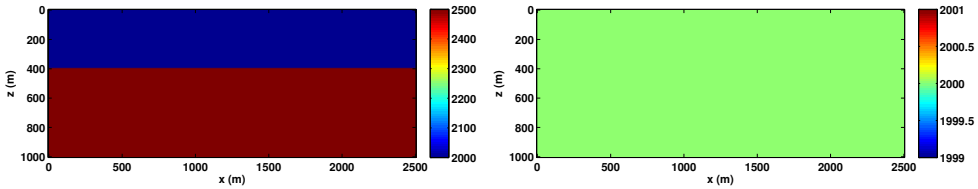

(a) (b)

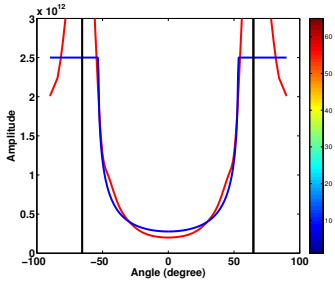

(c)

Figure 3: (a) Horizontal one-layer model overlay CIP location at $x = 1250$ m and $z = 400$ m indicated by star. (b) Modulus of angle-dependent reflectivity coefficients at CIP.

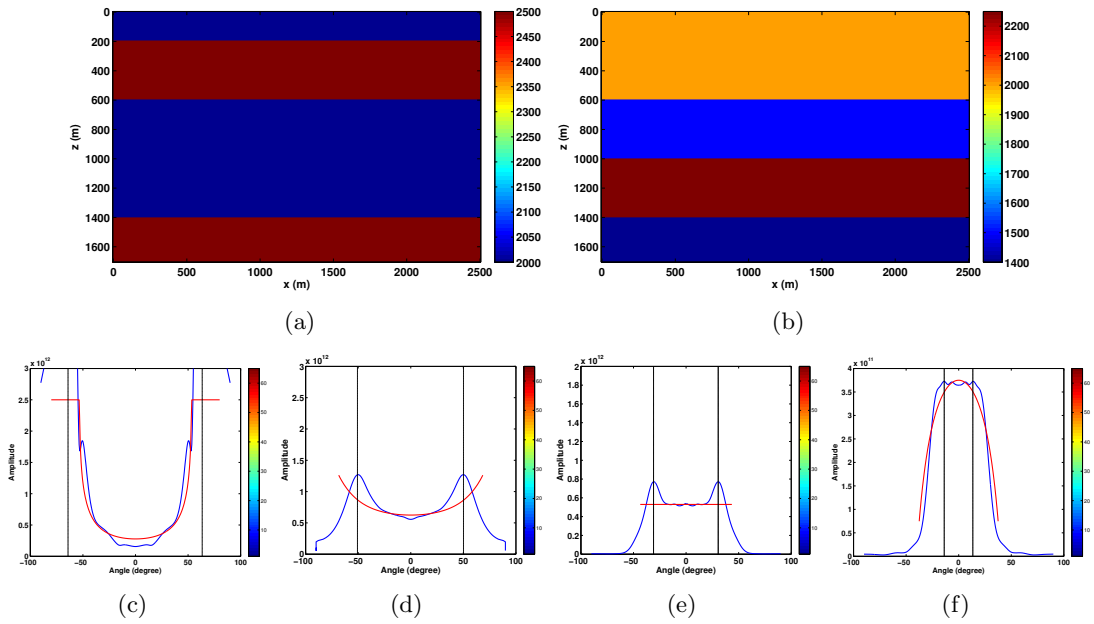

Figure 4: Angle dependent reflectivity coefficients in case of (a,b) horizontal four-layer model at $x = 1250$ m. The red curve is the theoretical reflectivity coefficients, blue curve is the wave-equation based reflectivity coefficients, and black curve is the critical-angle. (c) Modulus of angle-dependent reflectivity coefficients at $z = 200$ m. (d) Modulus of angle-dependent reflectivity coefficients at $z = 600$ m. (e) Modulus of angle-dependent reflectivity coefficients at $z = 1000$ m. (f) Modulus of angle-dependent reflectivity coefficients at $z = 1400$ m.

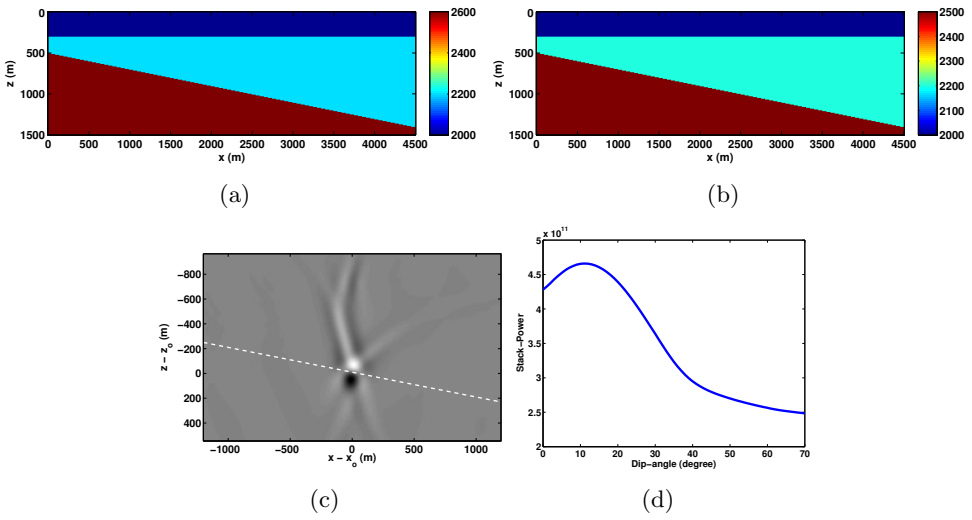

Figure 5: Estimation of local geological dip. (a,b) Two-layer model. (c) CIP gather at $x = 2250$ m and $z = 960$ m overlayed on dipping model. (d) Stack-power versus dip-angle. We can see that the maximum stack-power corresponds to the dip value of 11°, which is the true dip value.

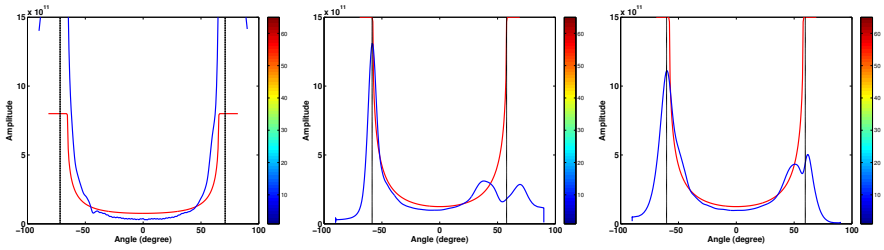

(a) (b) (c)

Figure 6: Modulus of angle-dependent reflectivity coefficients in two-layer model at $z = 300$ and 960 m and $x = 2250$ m. (a) Reflectivity coefficients at $z = 300$ m and $x = 2250$ m. Reflectivity coefficients at $z = 900$ m (b) with no dip $\theta = 0°$ and (c) with the dip obtained via the method described above ($\theta = 10.6°$).

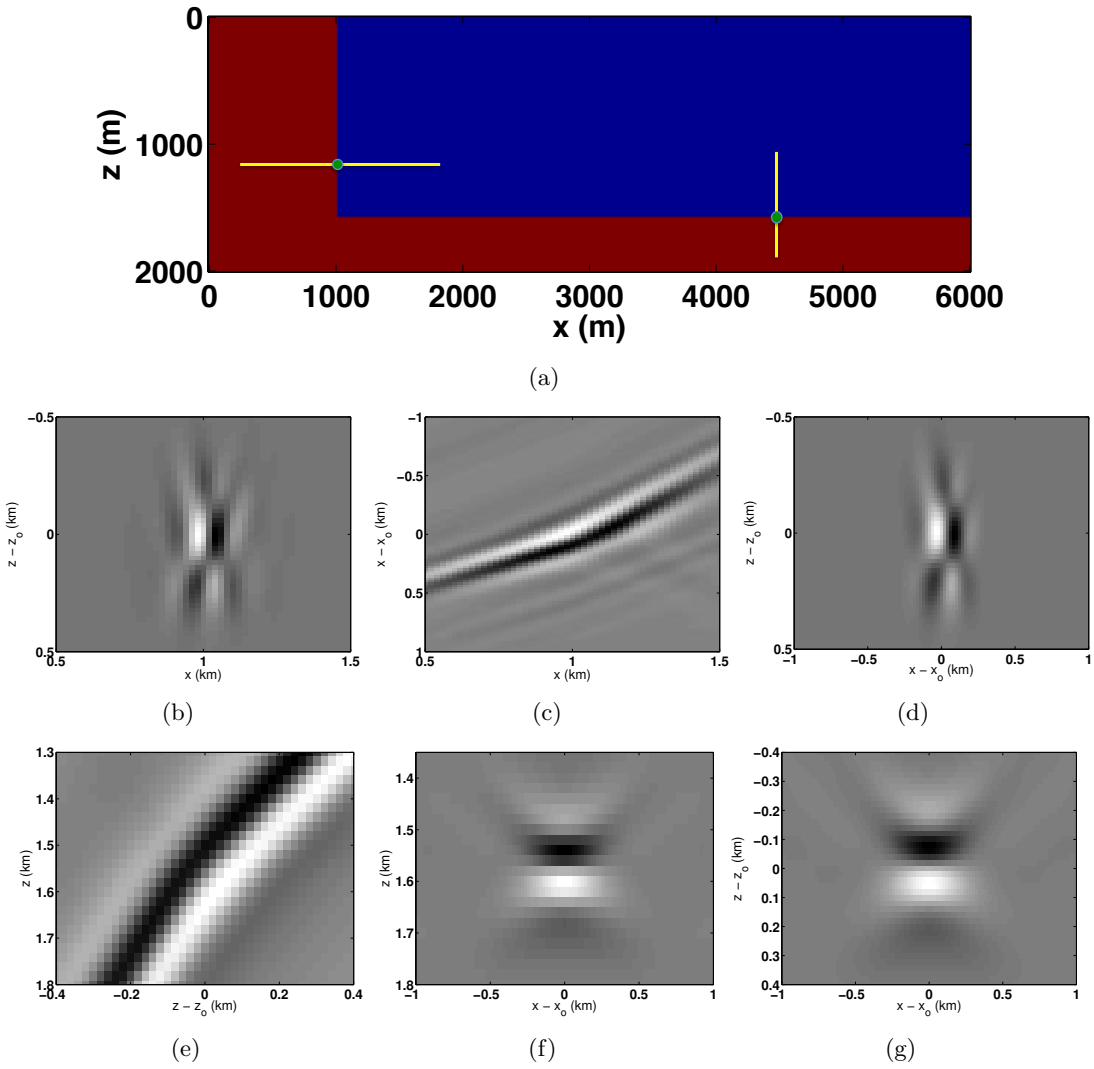

Figure 7: Comparison of working with CIGs versus CIPs. (a) True velocity model, where the yellow line indicates the location along which we computed the CIGs and the green dot is the location where we extracted the CIPs. (b,c) CIGs extracted along vertical and horizontal offsets directions in case of vertical reflector. (d) CIPs extracted along vertical ($z = 1.2$ km, $x = 1$ km) reflector. (e,f) CIGs extracted along vertical and horizontal offsets directions in case of horizontal reflector. (g) CIPs extracted along horizontal ($z = 1.5$ km, $x = 4.48$ km) reflector.

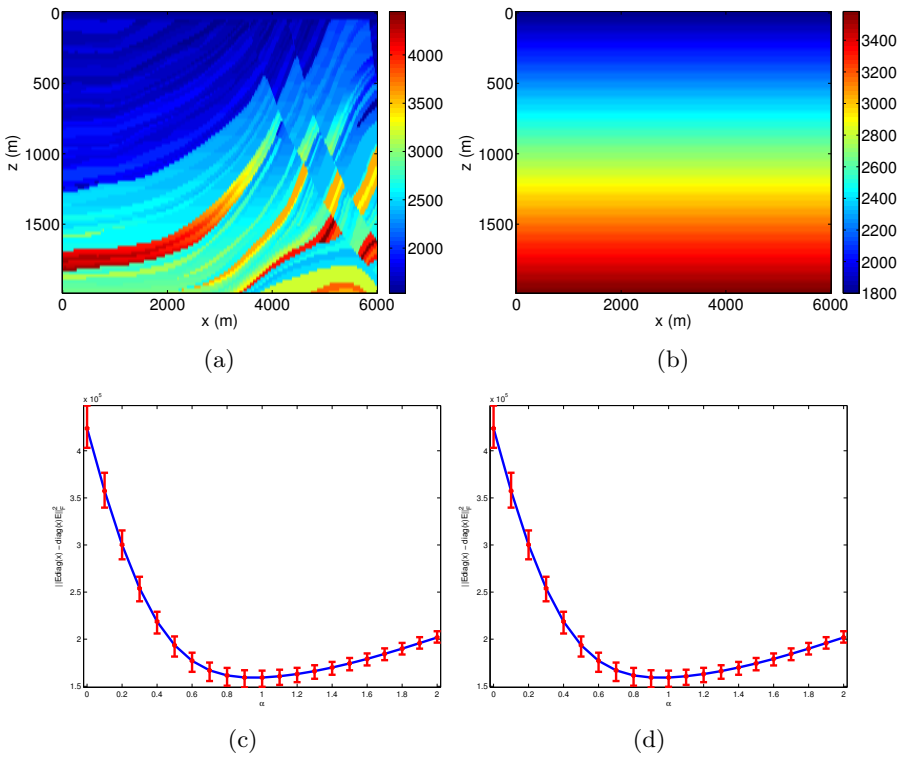

Figure 8: Randomized trace estimation. (a,b) True and initial velocity model. Objective functions for WEMVA based on the Frobenius norm, as a function of velocity perturbation using the complete matrix (blue line) and error bars of approximated objective function evaluated via 5 different random probing with (c) K=10 and (d) K = 80 for the Marmousi model.

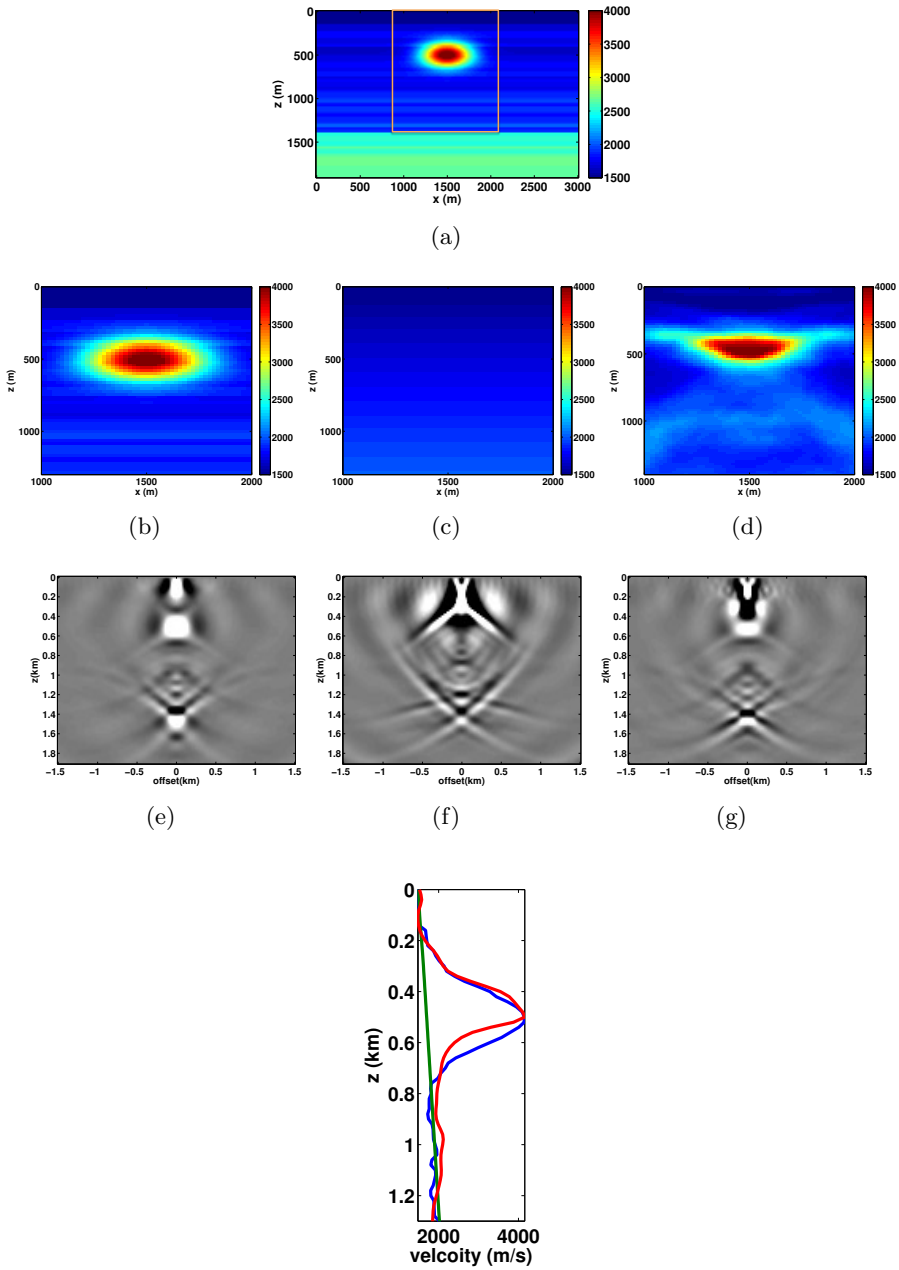

Figure 9: Lens model. (a,b,c) True model, initial model and inversion results after 30 iterations. (d,e,f) CIG along $x = 1500$ m and z for true model, initial model and inversion results. (g) Vertical trace profile extracted along $x = 1500$ m, (blue, green, red) True, Initial and inverted model.

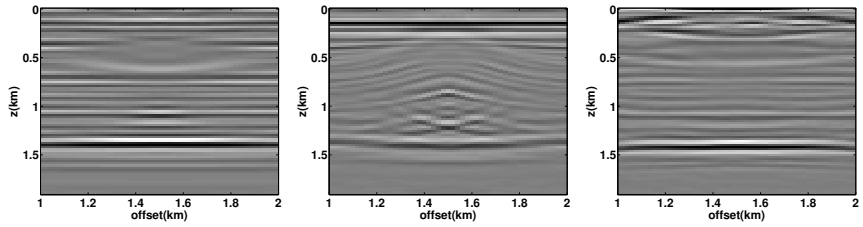

(a) (b) (c)

Figure 10: Least-square migration. Lens model. (a,b,c) True model, initial model and inversion results after 30 iterations. We can clearly see that WEMVA generated velocity model correctly repositioned the reflectors.

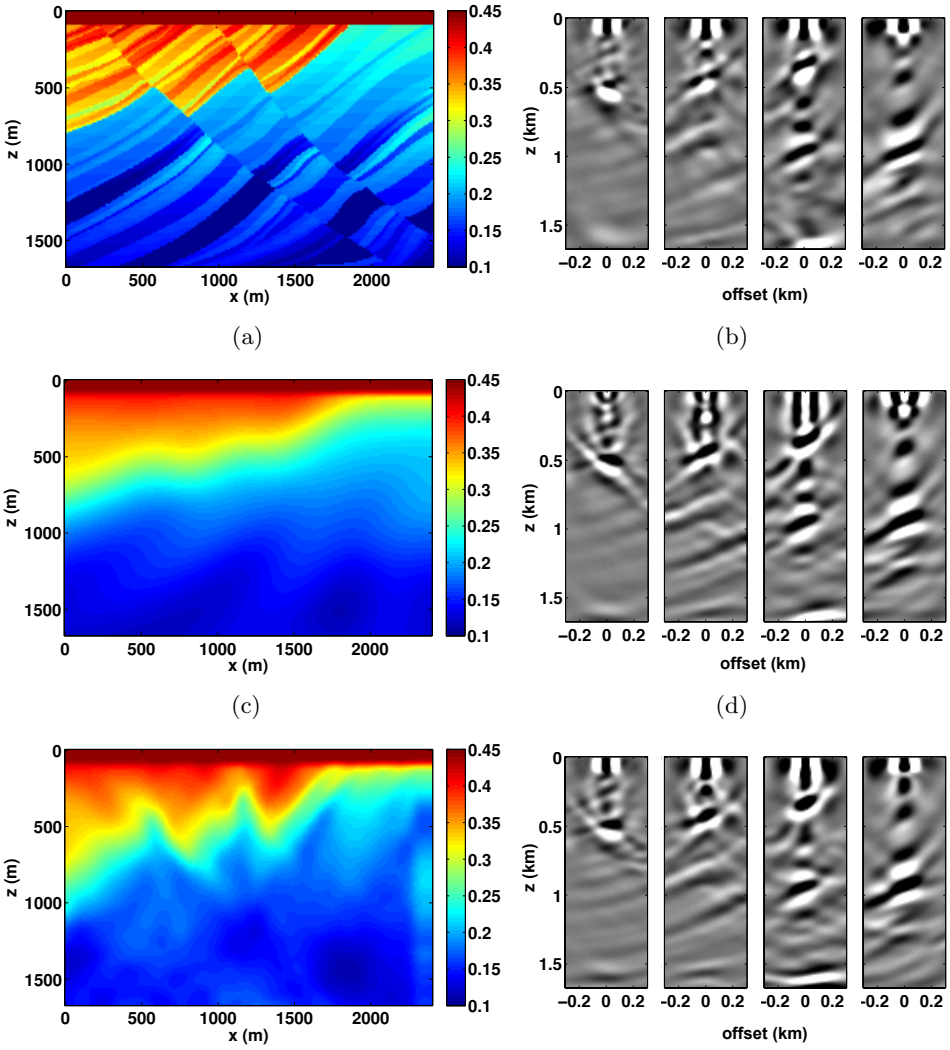

Figure 11: Marmousi model. (Left) True, Initial and Inverted model. (Right) CIG extracted along $x = 680$ m, 1160 m, 1640 m and 2220 m. (Top) True model. (Middle) starting model. (Bottom) Inverted results.

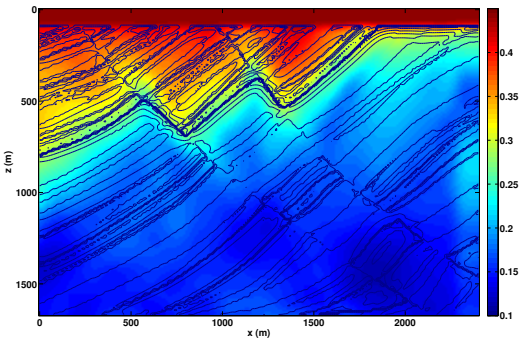

(a)

Figure 12: Marmousi model. WEMVA inversion results overlay with the contour plot, which representing the true velocity perturbation. We can clearly see that the updates in the velocity model matches the perturbation in the velocity model.

LIST OF TABLES

Table 1: Correspondence between continuous and discrete representations of the image volume. Here, ω represents frequency, $\mathbf{x}$ represents subsurface positions, and (i, j) represents the subsurface grid points. The colon (:) notation extracts a vector from e at the grid point i, j for all subsurface offsets.

	Continuous	Discrete
full image volume	$e(\omega_i, \mathbf{x}, \mathbf{x}')$	$\mathbf{E}_i$
migrated image	$\int_\Omega \mathrm{d}\omega\ e(\omega, \mathbf{x}, \mathbf{x})$	$\sum_{i=1}^{N_f} \mathsf{diag}(\mathbf{E}_i)$
CIP	$e(\omega_i, \mathbf{x}_j, \mathbf{x})$	$e_{i,j,:}$
	$e(\omega_i, \mathbf{x}, \mathbf{x}_k)$	$e_{i,:,k}$

	# of PDE solves	flops
conventional	$2N_s$	$N_s N_{h_x} N_{h_y} N_{h_z}$
this paper	$2N_x$	$N_r N_s$

Table 2: Computational complexity of the two schemes in terms of the number of sources N_{s}, receivers N_{r} sample points N_x and desired number of subsurface offsets in each direction $N_{h_{\{x,y,z\}}}$.

	time (s)	memory (MB)
conventional	23.6	103
this paper	2.02	0.03

Table 3: Comparison of the computational time (in sec) and storage memory (in megabytes) for computing CIP's gather on a very small model of size 50×50. We can see the significant difference in time and memory usage of the method proposed in this paper compared to the conventional method, even for a small test problem, and we expect this difference to be greatly exacerbated for realistically sized models.